

# Intelligent parameter decision-making and multi-objective prediction in multi-layer and multi-pass LDED process

Yaguan Li<sup>1,2</sup>, Zhenguo Nie<sup>2</sup>, Huilin Li<sup>2</sup>, Tao Wang<sup>1</sup>, Qingxue Huang<sup>1</sup>

<sup>1</sup> College of Mechanical Engineering, Taiyuan University of Technology, Shanxi, 030024, China

<sup>2</sup> Department of Mechanical Engineering, Tsinghua University, Beijing, 100084, China

<sup>3</sup> State Key Laboratory of Tribology in Advanced Equipment, Tsinghua University, Beijing, 100084, China

<sup>4</sup> Beijing Key Lab of Precision/Ultra-precision Manufacturing Equipments and Control, Tsinghua University, Beijing, 100084, China

**Abstract:** The main parameters that characterize the morphology quality of multi-layer and multi-pass laser metal printed parts are the surface roughness and the error between the actual printing height and the theoretical model height. This study employed the Taguchi method to establish the correlation between process parameter combinations and multi-objective characterization of metal print morphology quality (height error and roughness). The signal-to-noise ratio (SNR) and grey correlation analysis method were used to predict the optimal parameter combination for multi-layer and multi-pass printing: laser power 800 W, powder feeding rate 0.3 r/min, step distance 1.6 mm, scanning speed 20 mm/s. Subsequently, we constructed the Genetic Bayesian-back propagation network (GB-BP) to predict multi-objective responses. Compared with the traditional BP network, the GB-BP network improved the accuracy of predicting height error and surface roughness by 43.14% and 71.43%, respectively. The network can accurately predict the multi-objective characterization of the morphology and quality of multi-layer and multi-pass LDED metal printed parts.

**Key words:** Multi-layer and multi-pass laser cladding; Taguchi method; Grey relational analysis; GB-BP network

Laser-directed energy deposition (LDED) is a specific additive manufacturing technology that employs precise process parameters to produce solid workpieces. It facilitates surface modification of the workpiece through a specialized cladding layer to enhance its high temperature, wear, and corrosion resistance. Due to its inherited characteristics, such as high energy density, high efficiency, high design freedom, rapid construction speed, and exceptional physical and mechanical properties, LDED is extensively utilized in aerospace<sup>[1]</sup>, medical equipment<sup>[2]</sup>, and other large-sized components<sup>[3]</sup>. Metal powder is the most utilized raw material in this process, in which a nozzle injects the powder into the molten pool under the influence of a carrier gas before cooling it into shape.

With the rapid development of laser cladding technology<sup>[4]</sup>, the requirement for higher surface-forming quality of workpieces has increased, and the demand for shape and size deviations in multi-layer and multi-pass cladding processes has become more stringent.

The laser cladding process involves various parameters, in-

cluding laser spot diameter, laser power, powder-feeding rate, scanning speed, overlap rate, shielding gas flow rate, and powder-feeding gas flow rate. Different parameter combinations affect the forming quality of the printed parts<sup>[5][6][7]</sup>. Extensive research has been conducted on the influence of the single-layer cladding process on cladding height, cladding width, and cladding depth<sup>[8]</sup>, as well as the influence of process design on properties such as strength, hardness, high-temperature resistance, and corrosion resistance in the cladding layer<sup>[9][10][11]</sup>. Numerous experimental verifications are employed to analyze how different process parameters affect single-layer cladding<sup>[12]</sup>. Taguchi experiments, response surface methodology, and grey correlation analysis are always used to optimize parameters and predict responses<sup>[13][14]</sup>. Marzban et al.<sup>[15]</sup> conducted an orthogonal experiment and found the optimal solution by combining the principal component analysis (PCA) method with the TOPSIS technique for order preference by similarity to the ideal solution. Deng et al.<sup>[16]</sup> combined Taguchi and grey correlation analysis to opti-

Received date:

Foundation item: National Natural Science Foundation of China (52175237)

Corresponding author: Zhenguo Nie, Ph.D., Professor, E-mail: zhenguonie@tsinghua.edu.cn

Copyright © 2019, Northwest Institute for Nonferrous Metal Research. Published by Science Press. All rights reserved.

mize the multi-objective response parameters of the TiC particle-reinforced iron-based composite cladding layer prepared by pre-set powder laser cladding. Mondal et al.<sup>[17]</sup> conducted an orthogonal experiment to study the effects of laser power, scanning speed, and powder feeding rate on the quality of the cladding layer on the AISI1040 steel substrate and proposed a multi-objective response technology using grey correlation analysis to determine the optimal process parameters. Quazi et al.<sup>[18]</sup> adopted the Taguchi optimization method and used SNR response analysis and Pareto analysis of variance (ANOVA) to analyze the results. The optimal parameter combination obtained from the optimization process was experimentally tested, revealing significant improvements in surface hardness and roughness of the AA5083 cladding layer. Yu et al.<sup>[19]</sup> used the Taguchi grey correlation method to optimize the process parameters of laser cladding Fe313, selecting cladding width, height, and dilution rate as response targets. The results demonstrated that the optimized cladding layer improves morphology and structure compared to the unoptimized layer. Lian et al.<sup>[20]</sup> designed a Taguchi experiment to study the effects of process parameters on the microhardness and wear volume of the cladding layer to improve its performance. The grey correlation analysis method was used to determine the optimal process parameters and predict their grey correlation degree. The results showed that the average error between the predicted and experimental results was 5.3%. Lee et al.<sup>[21]</sup> investigated process parameters' impact on the geometry of AISI M4 single-pass laser cladding layers and employed response surface methodology to establish a mathematical model for predicting and controlling the layer's geometry. Alam et al.<sup>[22]</sup> utilized a central composite response surface methodology to design orthogonal experiments for investigating the influence of selected process parameters on the geometry and hardness of a single-pass laser cladding layer of AISI 420 metal powder. A multivariate regression model was also established to predict the cladding layer's hardness, the weld bead's aspect ratio, and the substrate's wetting angle. Bhardwaj et al.<sup>[23]</sup> studied the influence of process parameters (laser power, scanning speed, and powder feeding rate) on the cladding layer's geometric properties (dilution rate) based on the response surface method and variance analysis. The mapping relationship between parameters and geometric properties was established by regression modeling to find the optimal experimental parameters.

In addition to the aforementioned traditional methods, with the rapid development of machine learning, artificial neural networks, especially BP neural networks, have been widely used in laser cladding for process parameter optimization and multi-objective response prediction<sup>[24][25]</sup>. Li et al.<sup>[26]</sup> developed a BP neural network to predict the influence of process parameters on dilution rate, and the model's prediction error was 5.89%. However, this model is highly dependent on the size of the data set and is prone to falling into local minima when the

number of samples is limited. Swarm intelligence algorithms, such as genetic algorithms (GA)<sup>[27]</sup>, have strong global optimization capabilities. Therefore, many scholars have proposed combining GA with BP networks to solve the problems of slow GA convergence, falling into local minima, and achieving fast and accurate global optimization. Hanlou et al.<sup>[28]</sup> conducted a full factorial experiment to investigate the influence of process parameters on the geometric characteristics of Inconel 718 rails. They predicted the geometric characteristics of the cladding layer under different parameter combinations through linear regression and GA. Yang et al.<sup>[29]</sup> integrated BP and GA to establish a prediction model linking process parameters with the surface morphology quality of laser cladding layers and verified the accuracy of the model's prediction through experiments. Liu et al.<sup>[30]</sup> established a GA-BP neural network, using laser power, scanning speed, and powder thickness as process parameters; they conducted a full factorial experiment to produce a dataset and predicted the geometric characteristics of the single-layer, single-pass cladding layer of a high-power semiconductor laser. Yu et al.<sup>[31]</sup> designed an orthogonal experiment with overlap rate, powder feeding rate, and scanning speed as process parameters, and established a neural network model to predict the crack density of a high-hardness nickel-based laser cladding layer. The results were optimized using GA, and the model's reliability was validated through experimental verification. Deng et al.<sup>[32]</sup> designed a Taguchi experiment and used the SNR and variance analysis method to analyze the effects of laser power, spot diameter, overlap rate, and scanning speed on the microhardness of Ti(C, N) ceramic cladding layers. Furthermore, a BP neural network and quantum particle swarm optimization algorithm were employed to establish a mapping relationship between process parameters and responses for accurate prediction. Wang et al.<sup>[33]</sup> developed a powder-scale multi-physics model, which incorporates mass transfer, phase change, and heat transfer during the LDED process to predict the geometric characteristics of a single-layer, single-pass cladding track. In addition, a Gaussian regression model was established to predict the geometry of the cladding track under various parameter combinations.

The existing parameter optimization methods for LDED primarily focus on single-layer, single-pass, or single-layer multi-pass cladding, with limited research conducted on multi-layer and multi-pass cladding. However, due to the heat accumulation between layers, the manufacturing accuracy of multi-layer and multi-pass cladding is more sensitive to process parameters. However, when the orthogonal test involves many factors, it is difficult to determine the changing pattern of the test data. The optimal result is usually a combination of test parameters, which can neither accurately predict the height error and surface roughness nor obtain the optimal process parameters.

This study uses the Taguchi method to design orthogonal

experiments, analyzes the SNR of multi-objective responses, and uses the grey correlation analysis method to predict the optimal parameters for multi-layer and multi-pass printing so that the theoretical and actual height errors ( $\Delta H$ ) of the printed parts and the surface roughness ( $Ra$ ) are minimized. Experimental verification is carried out. After that, the GB-BP network is built to predict multi-objective responses.

## 1 Experimental materials and methods

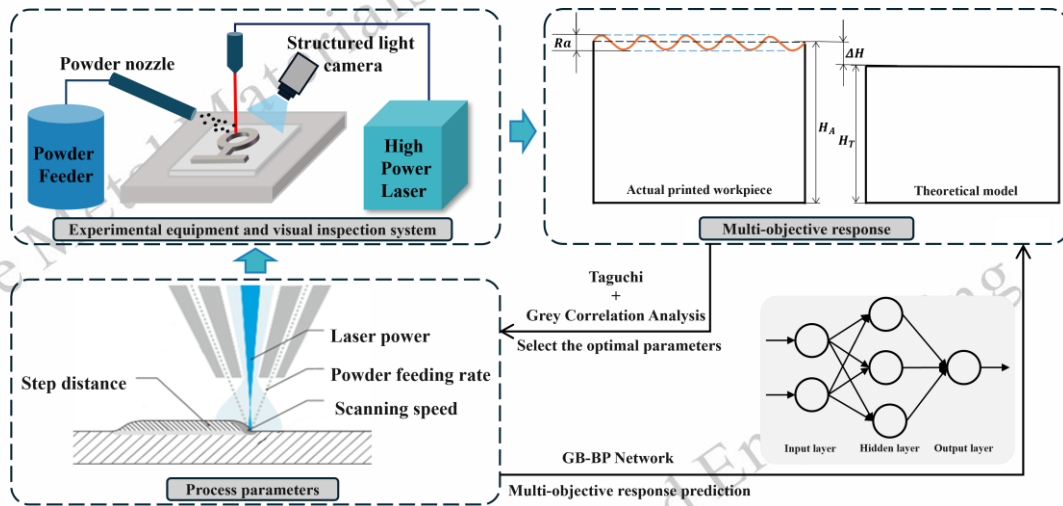


Fig.1 Schematic diagram of laser cladding system and method flow

### 1.1 Experimental materials and equipment

The printing equipment includes an optical platform, a three-axis motion system, a control console, a powder feeder, a laser, a powder feeder barrel, a water cooler, and a structured light camera, as shown in Fig.2. The structured light camera projects a specially designed pattern onto the surface of a three-dimensional object while utilizing an integrated camera to observe image distortion on the physical surface.

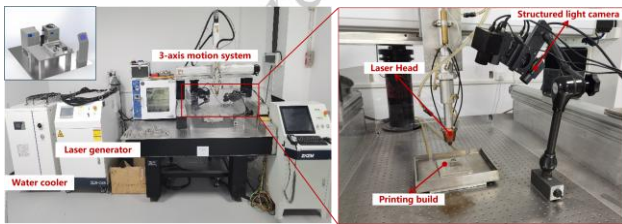


Fig.2 Dimensional adaptive correction system in the LDED process

The substrate used in the experiment is Fe316 stainless steel with a size of 100mm×100mm×8mm; the experiments were carried out using gas-atomized Fe316L powder with a particle size of 120~280 mesh by Carpenter Additive. Fe316L powder is mainly spherical, with delicate satellites attached to the surface of powder particles. The powder and substrate composition are confirmed using Energy Dispersive Spectroscopy (EDS), and the elemental composition is presented in Table 1. Before laser cladding, the metal powders were incubated in a drying oven at 100°C for two hours. The powder was then

Fig.1 illustrates the research approach, which includes laser cladding equipment and a visual inspection system. Point cloud data is collected to calculate the printed parts' height difference and surface roughness. A hybrid approach employing the Taguchi method and grey relational analysis is used to identify the optimal combination of parameters. Furthermore, the GB-BP network model is constructed for multi-objective response prediction.

loaded into a powder hopper before being deposited onto a substrate via laser cladding. Before deposition, the substrate surface was wiped with anhydrous ethanol for decontamination. After drying, the experiment was carried out.

Table 1 Substrate material and powder material composition list

Element	Fe	C	Cr	Si	Ni	Mn	Mo
Fe316L Mass%	Bal.	0.03	17.0	0.5	13.0	0.2	2.0
Fe316 Mass%	Bal.	0.06	18.16	0.49	8.05	1.06	0.11

The experiment used a laser cladding system with a maximum output power of 2000 W. The laser spot diameter is 2 mm, and high-purity argon was used as shielding and powder-feeding gas during cladding. After multi-layer laser cladding, an optical camera collected the 3D point cloud model of the component to calculate its  $\Delta H$  and  $Ra$ . Under ideal conditions, the surface coating after multi-lap cladding comprised convex peaks and concave valleys with relative regularity in the cross-section. Fig.3 illustrates the profile curve of this cross-section and the roughness  $Ra$  can be calculated by Eq.(1).

$$Ra = \frac{\int_0^L |z(x)| dx}{L} = \frac{1}{n} \sum_{i=1}^n |z_i| \quad (1)$$

where  $z_i$  is the longitudinal distance of the section profile;  $L$  is the transverse distance of the section contour;  $n$  is the number

of test points;  $z_i$  is the longitudinal distance of the cross-section profile of each test point.

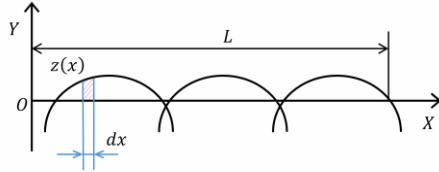


Fig.3 Sketch of ideal coating cross-section outline

The multi-layer, multi-pass laser deposition process gradually completes the forming or repairing of complex structures by depositing multiple layers (multiple superpositions) of metal materials in multiple passes (each melting path). The laser beam is focused on the metal surface and locally heats it to a molten state. The molten metal combines with the fed metal powder or wire to form a pool. In each layer, the melting trajectory of the laser molten pool scans along a predetermined path, and after each layer is completed, the deposited molten metal quickly cools and solidifies. The laser continues to act on the new layer to bond it to the previous layer metallurgically, and the whole process is repeated many times until the desired part shape is constructed. The repeated cross-scanning characteristics of this process place higher requirements on the scanning path and direction<sup>[34]</sup>. The filling path determines the internal structure of the printed model and, therefore, directly affects the strength and stability of the object.

The angle setting of linear filling impacts the strength, appearance, and stability of the printed parts in 3D printing. The angle of linear filling affects the strength of the printed parts in different directions. Usually, the strength direction of the printed part is parallel to the direction of the filling path. Common filling angle settings are  $0^\circ$ ,  $45^\circ$ ,  $90^\circ$ , and  $135^\circ$ , and the filling path at each angle provides different strength support. When filling at  $0^\circ$  and  $90^\circ$ , the printed parts perform well when subjected to lateral and longitudinal pressure.  $45^\circ$  and  $135^\circ$  filling provide balanced support in multiple directions. Due to the staggered layout of  $45^\circ$  and  $135^\circ$  angles, it can share strength in multiple directions and generally provide more uniform strength than horizontal or vertical filling<sup>[35]</sup>. Therefore, this work adopts the second filling method, as shown in Fig.4(a), and the multi-layer and multi-pass cladding effect is shown in Fig.4(b).

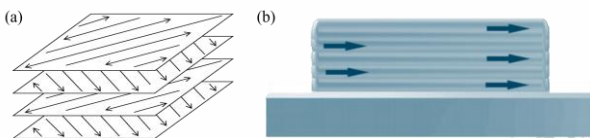


Fig.4 Schematic diagram of multi-layer and multi-pass cladding filling path and effect: (a) Fill path direction, (b) Multi-layer and multi-pass cladding.

## 1.2 Experimental design

In this study, laser power, powder feeding rate, step distance, and scanning speed were selected as the factors influencing the flatness of the component's top surface. Table 2 lists these four factors and their corresponding levels. The  $L_{(16)}(4^4)$  Taguchi orthogonal experimental design was adopted, with the orthogonal table presented in Table 3. Two response items,  $\Delta H$  and  $Ra$ , were selected to evaluate the printing quality and obtain a multi-layer cladding workpiece with excellent comprehensive performance.

Table 2 Process parameters of laser cladding and their levels

Parameters	Notations	Level1	Level2	Level3	Level4
Laser power (W)	LP	800	900	1000	1100
Powder feeding rate (r/min)	PR	0.3	0.4	0.5	0.6
Step distance (mm)	SD	1.0	1.2	1.4	1.6
Scanning speed (mm/s)	SS	16	18	20	22

## 2 Results and discussion

### 2.1 Experiment results

Different combinations of process parameters will result in different thicknesses of the cladding layer. Therefore, it is imperative to determine the single-layer cladding thickness corresponding to each parameter combination before multi-layer cladding. The 16 sets of parameters in Table 3 were used for laser cladding, and the single-layer  $H_l$  cladding height was measured as the benchmark thickness for multi-layer cladding.

Table 3  $L_{(16)}(4^4)$  Taguchi orthogonal experimental design

No.	LP (W)	PR (r/min)	SD (mm)	SS (mm/s)
1#	900	0.6	1.0	16
2#	1000	0.4	1.2	16
3#	800	0.6	1.2	20
4#	1100	0.3	1.2	18
5#	800	0.5	1.0	18
6#	900	0.5	1.2	22
7#	1000	0.3	1.0	22
8#	1100	0.4	1.0	20
9#	800	0.3	1.4	16
10#	1000	0.5	1.4	20
11#	1100	0.6	1.4	22
12#	900	0.4	1.4	18
13#	1100	0.5	1.6	16
14#	900	0.3	1.6	20
15#	1000	0.6	1.6	18
16#	800	0.4	1.6	22

Fig.5 illustrates the experimental results of cladding a single layer, and Table 4 provides the thickness of the cladding layer corresponding to each set of parameters.

The heights were used as the base heights for 16 parameter combinations, and multi-layer cladding was performed. The experimental results are shown in Fig.6. Due to the installation limitations of the measuring equipment, our current printing height can reach 20mm. It is reasonable to use  $\delta H$  to characterize it within this range. In principle, this method is also valid for high printing thicknesses. Table 5 lists the measurement results of the two responses of all specimens.

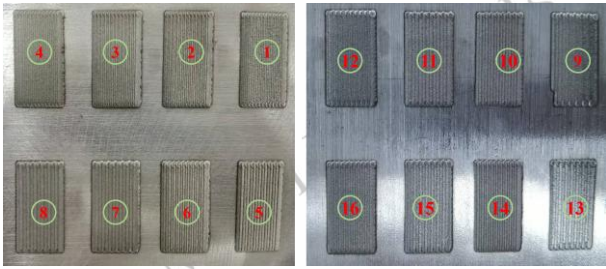


Fig.5 16 sets of parameters for single layer cladding experiment

Table 4  $H_1$  corresponding to different parameter combinations

No.	$H_1$	No.	$H_1$	No.	$H_1$	No.	$H_1$
1#	0.97	5#	1.48	9#	0.39	13#	0.35
2#	0.71	6#	1.32	10#	0.57	14#	0.50
3#	0.82	7#	0.38	11#	0.70	15#	0.45
4#	1.22	8#	0.73	12#	0.61	16#	0.18

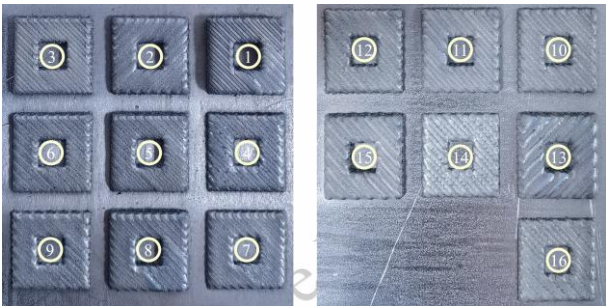


Fig.6 16 sets of parameters for multi-layer cladding experiments

Table 5 Measurement results of  $\Delta H$  and  $Ra$  for multilayer cladding

No.	$\Delta H(\text{mm})$	$Ra(\text{mm})$	No.	$\Delta H(\text{mm})$	$Ra(\text{mm})$
1#	2.3442	0.3145	9#	0.9551	0.0825
2#	1.0478	0.2003	10#	1.4096	0.1104
3#	0.8859	0.1395	11#	1.4056	0.1369
4#	3.7846	0.1372	12#	0.8691	0.1128
5#	3.4965	0.2191	13#	2.8770	0.1309
6#	3.5757	0.1538	14#	0.0343	0.0974
7#	1.1789	0.1130	15#	2.7508	0.1331
8#	0.5584	0.2102	16#	1.8251	0.0850

Extract the printed part's top layer point cloud model and perform the plane fitting. As shown in Fig.7, calculate the distance from the plane to the substrate as the actual printing height and subtract it from the theoretical height to get the

height error. Calculate the distance from all points of the top layer point cloud to the plane and calculate the average value, which is the surface roughness of the printed part. When conducting experimental measurements, high-precision measuring equipment was used to ensure the accuracy of the measured data. The possible error range when characterizing roughness is the measurement error caused by the equipment, which is less than 0.01mm.

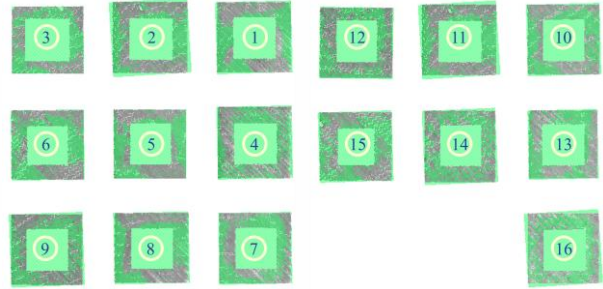


Fig.7 Result of the top layer plane fitting of the printed part

## 2.2 Calculation of the SNR for each response and Taguchi analysis

SNR is introduced as an evaluation index. According to specific requirements, the SNR characteristics are divided into larger, smaller, and nominal values, corresponding to the target values of maximizing, minimizing, and reaching or approaching the quality response. Eq.(2)-Eq.(4) presents the calculation formula.

$$SNR = -10 \log \left( \frac{1}{n} \sum_{i=1}^n \frac{1}{y_i^2} \right) \quad (2)$$

$$SNR = -10 \log \left( \frac{1}{n} \sum_{i=1}^n y_i^2 \right) \quad (3)$$

$$SNR = -10 \log \left( \frac{1}{n} \sum_{i=1}^n (y_i - m)^2 \right) \quad (4)$$

where SNR is the quality characteristic,  $n$  is the number of experiments,  $m$  is the experimental target value, and  $y_i$  is the experimentally measured data. The responses  $\Delta H$  and  $Ra$  are as small as possible. Thus, Eq.(3) is employed to calculate the SNR of these two responses. Table 6 lists the SNR corresponding to each group of experiments.

Table 6 SNR of response targets

No.	$\Delta H(\text{mm})$	$Ra(\text{mm})$	No.	$\Delta H(\text{mm})$	$Ra(\text{mm})$
1#	-7.400	10.046	9#	0.4399	21.670
2#	-0.406	13.964	10#	-2.982	19.138
3#	1.052	17.110	11#	-2.957	17.271
4#	-11.560	17.252	12#	1.219	18.952
5#	-10.873	13.187	13#	-9.179	17.660
6#	-11.067	16.261	14#	29.294	20.227
7#	-1.430	18.938	15#	-8.789	17.517
8#	5.061	13.549	16#	-5.226	21.414

The mean SNR values for each level are calculated using

Eq.(5) to assess the effect of different factor levels on the blade surface properties. The factor level yielding the highest mean SNR indicates the optimal level for that particular factor.

$$R_{xi} = \frac{1}{k} \sum_{i=1}^k (SNR_i) \quad (5)$$

where  $R_{xi}$  is the mean value of the SNR corresponding to each factor level,  $SNR_i$  is the SNR containing the associated level, and  $k$  is the number of experiments.

**Table 7 Response table of SNR for  $\Delta H$  and  $Ra$**

Level	$\Delta H(\text{mm})$				$Ra(\text{mm})$			
	LP	PR	SD	SS	LP	PR	SD	SS
1	-3.66	4.17	-3.66	-4.15	18.35	19.52	13.93	15.83
2	3.01	0.16	-5.49	-7.50	16.37	16.97	16.15	16.73
3	-3.40	-8.52	-1.08	8.11	17.39	16.56	19.26	17.51
4	-4.66	-4.52	1.53	-5.17	16.43	15.49	19.20	18.47
Delta	7.67	12.70	7.02	15.61	1.97	4.04	5.33	2.64
Rank	3	2	4	1	4	2	1	3

The extreme deviation is the difference between the highest and lowest average response values of the factor level's SNR. It quantifies the relative impact of different factor levels on experimental outcomes. The larger the extreme deviation, the more significant the influence of that factor. Table 7 shows each level's average SNR value responses for various aspects. Fig.8 illustrates the trends in SNR for each factor along with the two corresponding responses  $\Delta H$  and  $Ra$ . The SNR analysis reveals that the optimal parameters for obtaining the minimum  $\Delta H$  and  $Ra$  are LP1PR1SD3SS4 and LP2PR1SD4SS3, respectively.

According to the ranking analysis results of SNR, each process parameter influences the height error  $\Delta H$  of the top layer:  $SS > PR > LP > SD$ . For the cladding layer height, scanning speed is the most influential factor. If the scanning speed is too slow, the prolonged residence of the laser head in the molten pool leads to an increased transfer of heat energy to either the substrate or the pre-ceding cladding layer, resulting in a progressively higher cladding layer height that surpasses its theoretical value. If the scanning speed is excessively high, the nozzle injects a reduced amount of metal powder into the molten pool, diminishing the heat energy transferred to the powder. As a result, the cladding layer height is less than its theoretical value. Therefore, selecting an appropriate scanning rate can mitigate height errors and improve the quality of the printed part.

According to the ranking analysis results of SNR, each process parameter influences the surface roughness  $Ra$  of the top layer:  $SD > PR > SS > LP$ . The roughness of the top surface is mainly affected by the overlap ratio, which is the parameter moving step distance selected in this paper. When the step distance is too small, the overlap area between the cladding layers increases, which may cause excessive material to

accumulate in a specific area, resulting in protrusions or wavy shapes on the surface and increasing the surface roughness. In addition, the heat is concentrated in the overlapping area, which may cause thermal deformation or burning of the cladding material, resulting in microcracks or defects, further increasing the roughness. When the step distance is too large, due to the failure of the cladding material to fully cover, the overlap between the cladding layers is insufficient, which may cause local areas to fail to fuse fully, resulting in local weak areas, resulting in an uneven surface, thereby increasing the roughness. In addition, insufficient overlap may cause the bonding strength between the cladding layers to decrease, and peeling or flaking may occur easily, affecting the overall flatness of the surface. This is consistent with the conclusions of existing research work<sup>[36]</sup>. Choosing a suitable overlap rate, that is, the step distance, can make the surface unevenness of the workpiece flat, thereby significantly reducing its roughness.

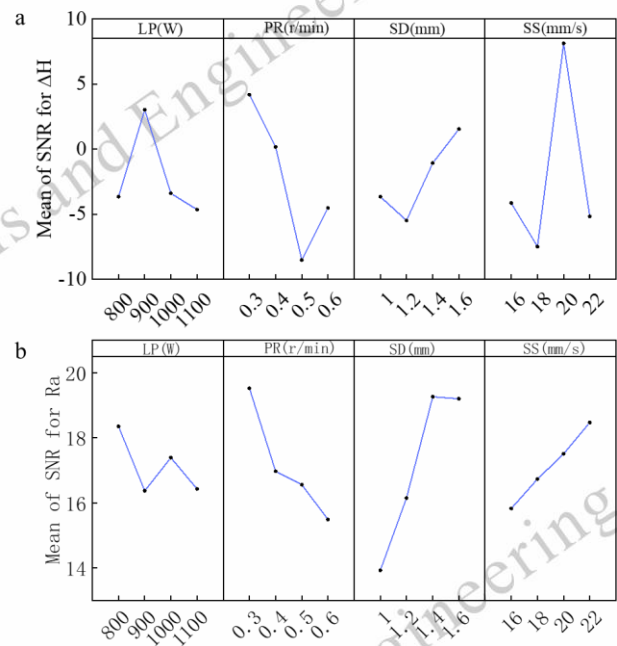


Fig.8 Main effect plot for the SNR analysis of responses:(a)  $\Delta H$ , (b)  $Ra$

### 2.3 Multi-objective optimization by grey relational analysis

The Taguchi method is a single-objective response optimization method, while this paper aims to optimize two objectives simultaneously. Therefore, the grey correlation theory is introduced for multi-objective optimization to determine the optimal laser cladding parameters. The grey correlation theory effectively integrates multiple targets into one objective by converting individual responses into grey relational grades (GRG)<sup>[37]</sup>.

Grey relational analysis requires a series of calculations<sup>[38]</sup>.

The first is data normalization. Since each response's numerical range and unit are different, it is necessary to normalize it. Eq.(6) is calculated so that the data is between 0 and 1, and its scale remains unchanged. The normalized results are shown in Table 8.

$$X_i(k) = \frac{Y_i(k) - \min Y_i(k)}{\max Y_i(k) - \min Y_i(k)} \quad (6)$$

where  $Y_i(k)$  is the SNR for the response  $k$  ( $k = 1, 2$ ) of experiment  $i$  ( $i = 1, 2, \dots, 16$ ),  $\max Y_i(k)$  and  $\min Y_i(k)$  is the maximum and minimum value of the response  $k$  among all 16 experiments,  $X_i(k)$  is the normalized value of the experiment  $i$  and response  $k$ .

**Table 8 The normalized SNR value of response targets**

No.	$\Delta H$ (mm)	$Ra$ (mm)	No.	$\Delta H$ (mm)	$Ra$ (mm)
1#	0.102	0.000	9#	0.293	1.000
2#	0.273	0.337	10#	0.210	0.782
3#	0.309	0.608	11#	0.211	0.622
4#	0.000	0.620	12#	0.313	0.766
5#	0.017	0.270	13#	0.058	0.655
6#	0.012	0.535	14#	1.000	0.876
7#	0.248	0.761	15#	0.068	0.643
8#	0.407	0.301	16#	0.155	0.978

Then, the grey relational coefficient ( $GRC$ ) is calculated by Eq.(7)<sup>[38]</sup>.

$$GRC_i(k) = \frac{\min_i |x_i^0 - x_i(k)| + \xi \max_i |x_i^0 - x_i(k)|}{|x_i^0 - x_i(k)| + \xi \max_i |x_i^0 - x_i(k)|} \quad (7)$$

where  $GRC_i(k)$  is the  $GRC$  for the response  $k$  ( $k = 1, 2$ ) of experiment  $i$  ( $i = 1, 2, \dots, 16$ ),  $x_i^0$  is the ideal value of experiment  $i$  ( $i = 1, 2, \dots, 16$ ) and satisfies  $x_i^0 = 1$  in this work,  $\xi$  is the distinguishing coefficient over the range  $0 < \xi < 1$ . In this study, we set  $\xi = 0.5$  by comprehensively considering effect and stability<sup>[16]</sup>.  $GRC$  is the relationship between the actual normalized SNR and the ideal values, where the ideal values are all 1000. Finally, the integrated  $GRG$  calculation using Eq.(8)<sup>[38]</sup>.

$$GRG_i = \frac{1}{n} \sum_{k=1}^n GRC_i(k) \quad (8)$$

where  $GRG_i$  is the  $GRG$  of experiment  $i$  ( $i = 1, 2, \dots, 16$ ),  $n$  is the number of the responses, and  $n = 2$  in this work. Eq.(8) can equally weigh the importance of  $\Delta H$  and  $Ra$ .

Each process parameter's grey correlation coefficient and correlation level are calculated, as shown in Table 9. We introduced the Taguchi method into the grey correlation analysis to obtain a parameter combination with good printing quality. Fig.9 shows the central effect diagram of  $GRG$ . According to the study, the best process parameter combination is LP1PR1SD3SS3. The laser power is 800 W, the powder feeding speed is 0.3 r/min, the step distance is 1.6 mm, and the printing speed is 20 mm/s.

**Table 9 Grey relational analysis data table for responses**

No.	GRC		GRG		No.	GRC		GRG	
	$\Delta H$	$Ra$	Values	Rank		$\Delta H$	$Ra$	Values	Rank
1#	0.358	0.333	0.345	16	9#	0.414	1.000	0.707	2
2#	0.408	0.430	0.419	14	10#	0.388	0.679	0.542	5
3#	0.420	0.560	0.490	7	11#	0.388	0.569	0.478	8
4#	0.333	0.568	0.451	11	12#	0.421	0.681	0.551	4
5#	0.337	0.407	0.372	15	13#	0.347	0.592	0.469	9
6#	0.336	0.518	0.427	13	14#	1.000	0.801	0.814	1
7#	0.399	0.680	0.540	6	15#	0.349	0.583	0.466	10
8#	0.457	0.417	0.437	12	16#	0.372	0.958	0.665	3

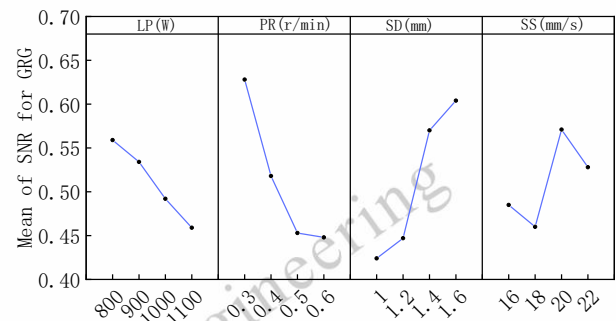


Fig.9 Main effect plot for the SNR analysis of  $GRG$ .

**Table 10 Response table for SNR of  $GRG$**

Level	LP	PR	SD	SS
1	0.559	0.628	0.424	0.485
2	0.534	0.518	0.447	0.460
3	0.492	0.453	0.570	0.571
4	0.459	0.448	0.604	0.528
Delta	1.434	2.846	2.958	1.707
Rank	4	2	1	3

In addition, Table 10 shows the factors' importance to the grey correlation degree as  $SD > PR > SS > LP$ . The step distance plays a leading role in the height error and roughness.

## 2.4 Experimental verification of optimal parameters

An additional verification experiment is necessary since the optimal parameter combination was not involved in the  $L_{16}(4^4)$  experiment table. Eq.(9)<sup>[38]</sup> can predict grey relational grades.

$$GRG_p = GRG_m + \sum_{j=1}^n (GRG_j - GRG_m) \quad (9)$$

where  $GRG_m$  is the mean value of total  $GRG$ ,  $n$  is the number of process parameters and  $n = 4$  in this work,  $GRG_j$  is the mean value of all the  $GRG$  for processing parameter  $j$  ( $j = 1, 2, 3, 4$ ) at the optimal level,  $GRG_p$  is the predicted  $GRG$  at the selected level.

At the optimal process parameters, the predicted value of  $GRG$  is 0.828. Comparing the results of the single-target response of  $\Delta H$  and  $Ra$  with the grey correlation method analysis results, it can be seen that the prediction results of  $GRG_{pre}$

and the experimental calculation result in  $GRG_{Exp}$  are consistent in size trend, as shown in Table 11. It is further explained that the parameters obtained by the grey correlation analysis of multi-target response are optimal.

**Table 11 Comparison of single-target response and multi-target response results**

Level	$\Delta H$	$Ra$	$\Delta H + Ra$
LP(W)	800	900	800
PR(r/min)	0.3	0.3	0.3
SD(mm)	1.4	1.6	1.6
SS(mm/s)	22	20	20
$GRG_{Exp}$	0.719	0.721	0.807
$GRG_{Pre}$	0.751	0.804	0.828

## 2.5 Multi-objective prediction based on GB-BP network

Due to the complexity of the metal LDED process and the inherent variability in product requirements, it is not advisable to conduct individual experiments. Therefore, a mapping relationship between process parameter combinations and responses should be established based on a few samples. Artificial Neural Network (ANN) is a computational model miming biological neural networks<sup>[39]</sup>. Its architecture includes an input layer that receives input data, multiple hidden layers that process and extract features from the input data, and an output layer that generates the final result. The BP network is the most widely used ANN model<sup>[40]</sup>. The back-propagation algorithm optimizes the network's weights and biases to improve the model's accuracy. The structural diagram is shown in Fig.10. This method establishes the correlation between input process parameters (laser power, powder feeding rate, step distance, scanning speed) and output parameters (surface roughness, height difference).

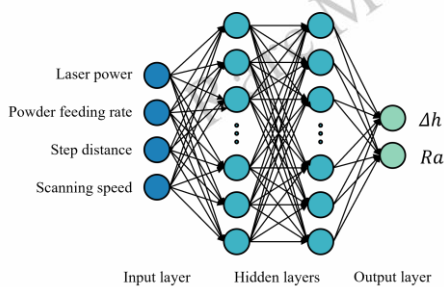


Fig.10 BP network topology diagram

The appropriate number of neurons enhances the network's prediction accuracy. Bayesian optimization (BO) determines the optimal configuration, including hidden layers, neurons, and network learning rate<sup>[41]</sup>. BO constructs a Gaussian process probability model to represent the possible distribution of the objective function.

**Table 12 The parameters of the BP network**

Parameters	Value
Activation function	Sigmoid
Optimizer	Adam
Epochs	600
Learning rate	0.027
The number of hidden layers	2
Number of nodes in the first hidden layer	10
Number of nodes in the second hidden layer	6

The model is updated by randomly selecting a set of points to be evaluated. From there, new evaluation points are identified and added to the model for iteration. Repeat the above process until reaching the maximum number of iterations or converging to a predetermined level of accuracy. The parameters of the BP network we selected are shown in Table 12. The initial 14 data sets from Table 5 are the training set, and the last two are the testing set.  $RMSE$  is used to evaluate network performance, as shown in Eq.(10).

$$RMSE = \sqrt{\frac{1}{n} \sum_{i=1}^n (Y_i - \hat{Y}_i)^2} \quad (10)$$

where  $n$  is the number of samples,  $Y_i$  is the ground truth for each data set, and  $\hat{Y}_i$  is the predicted output of the network.

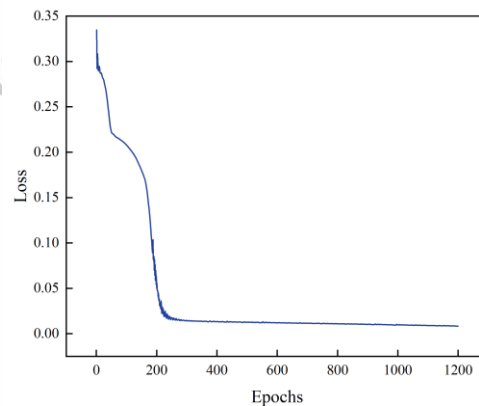


Fig.11 The loss function curve of the BP network

Fig.11 illustrates the loss function curve. The prediction results are shown in Fig 13(a) and (b). The relative prediction errors of  $\Delta H$  and  $Ra$  were calculated to be 51% and 21%, respectively, as shown in Table 14. The relative error of  $\Delta H$  is higher than 50%, indicating that its prediction performance is not ideal. The BP network is prone to fall into the local optimum, resulting in an unsatisfactory training effect. In addition, overfitting will occur when the training data is insufficient, decreasing the model's generalization ability for new data.

GA mimics the natural process of biological evolution, employing selection, crossover, and mutation operations to search for optimal solutions. It initializes a population to explore the solution space to handle multiple problems and optimize multiple parameters simultaneously<sup>[42]</sup>. Consequently, the GA was introduced as a replacement for the backpropaga-

tion process in the BP network, enabling accurate prediction of multiple responses<sup>[44]</sup>. The algorithm flowchart is shown in Fig.12. The weights and biases of the BP network are encoded as chromosomes, with their values constrained within  $[-1,1]$ . The fitness function is the mean square error ( $MSE$ ), denoted by Eq.(11). The GB-BP parameters were determined through experiments, as shown in Table 13.

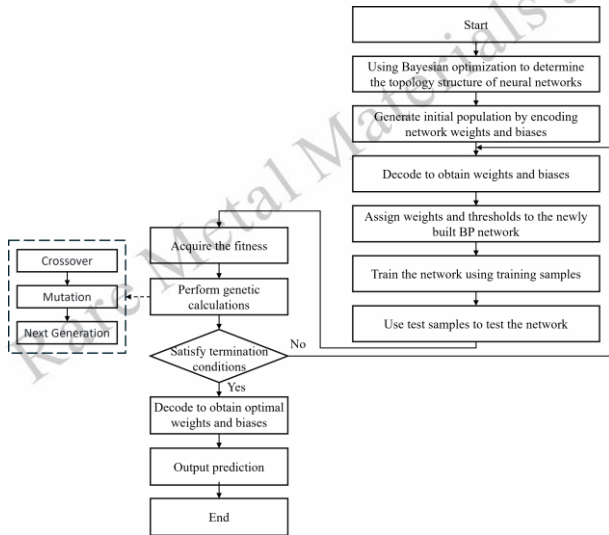


Fig.12 The flow chart of the GB-BP network

$$MSE = \frac{1}{n} \sum_{i=1}^n (Y_i - \hat{Y}_i)^2 \quad (11)$$

where  $n$  is the number of test sets,  $Y_i$  is the ground truth and  $\hat{Y}_i$  is the network predict value.

Table 13 The parameters of the GB-BP network

Parameters	Value
Coding method	Real number coding
Max iteration	6000
Population size	80
Elite ratio	0.06
Parents portion	0.5
Crossover probability	0.54
Mutation probability	0.01
Crossover type	Uniform
Number of nodes in the first hidden layer	10
Number of nodes in the second hidden layer	6

Similarly to the BP network, we selected the first 14 data sets from Table 5 as the training set and the last two as the testing set. Fig.13 illustrates the loss function curve. It can be seen that the loss function is much smoother than that of the BP network. This is because, after the introduction of GA, BP can adjust the network weights according to the gradient based on GA optimization to fine-tune the model and avoid loss fluctuations caused by overfitting. Secondly, GA does not rely on the learning rate. It determines the direction and amplitude

of weight updates through the evolution process, which makes the training process more stable. Fig.14(c) and (d) show the GB-BP network's prediction results. The relative prediction errors of  $\Delta H$  and  $Ra$  were calculated to be 29% and 6%, respectively, as shown in Table 14. The results show that the prediction error of  $\delta h$  is larger than that of  $Ra$ . The main reason is that compared with  $Ra$ , the response of  $\Delta H$  has a smaller correlation coefficient with several process parameters mentioned in the paper. In addition, the prediction of the network itself is based on a small sample training model. If the number of samples in the training set is appropriately increased, the prediction accuracy will be improved to a certain extent.

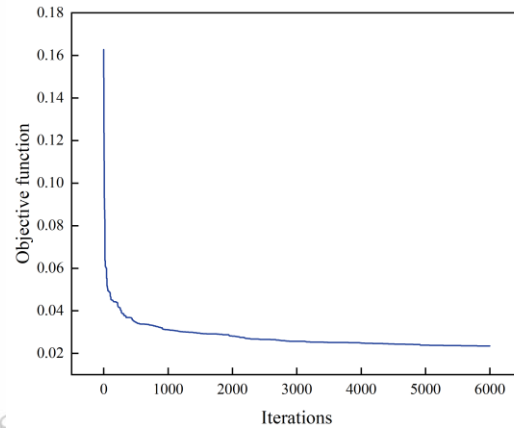


Fig.13 The objective function curve of the GB-BP network

Table 14 Comparison of relative error between BP network and GB-BP network prediction results.

	$Ra$ (mm)		$\Delta H$ (mm)	
	BP	GB-BP	BP	GB-BP
Relative error	51%	29%	21%	6%

It is evident that compared to the BP network, the relative error of GB-BP network prediction is significantly reduced, and the prediction accuracy is greatly improved. Compared with the traditional BP network, the GB-BP network has improved the accuracy of predicting  $\Delta H$  and  $Ra$  by 43.14% and 71.43%, respectively.

Table 15 GB-BP network cross-validation results

No.	Relative error		No.	Relative error	
	$\Delta H$	$Ra$		$\Delta H$	$Ra$
1#	40%	19%	5#	44%	18%
2#	37%	19%	6#	64%	13%
3#	26%	19%	7#	38%	18%
4#	33%	29%	8#	52%	18%

The k-fold cross-validation method was used to verify the generalization ability of the GB-BP network<sup>[43]</sup>. The data was divided into eight folds, each containing two data groups. Every time, seven folds (fourteen groups of data) were used for training, and one fold (two groups of data) was used for

verification, totaling eight training and verification. The results are shown in Table 15. The results show that the average relative error of the GB-BP network in predicting  $\Delta H$  is 42%, and the average relative error of the GB-BP network in predicting  $Ra$  is 19%, much smaller than the prediction results of the BP network. It is proved that the GB-BP network can ac-

curately predict multiple responses and has good generalization ability.

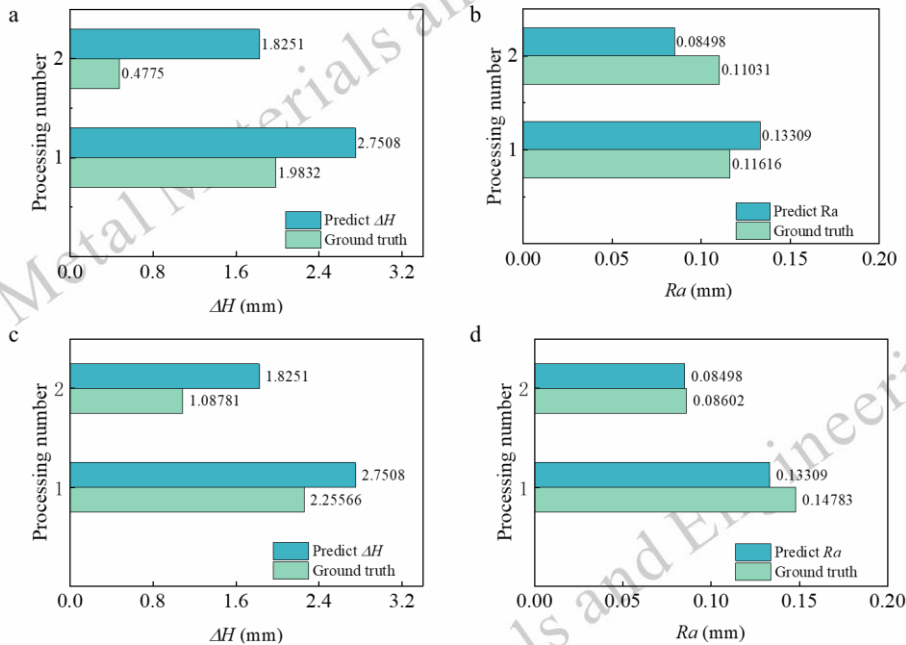


Fig.14 Comparison between the results predicted by BP and GB-BP networks. (a) The BP network predicts the value of  $\Delta H$  (b) The BP network predicts the value of  $Ra$  (c) The GB-BP network predicts the value of  $\Delta H$  (d) The GB-BP network predicts the value of  $Ra$ .

### 3 Conclusions

This paper used the Taguchi method to study the effects of process parameters such as laser power, powder feeding rate, step distance, and scanning speed on the height error and surface roughness of printed parts through signal-to-noise ratio analysis. Grey correlation analysis was used to achieve synchronous multi-objective optimization, and a GB-BP network model was established to predict multi-objective responses. The conclusions of the research are as follows:

(1). Build a visual inspection system and calculate the height error and surface roughness between the point cloud model of the printed part and the theoretical model through collection and analysis as performance parameters to characterize the surface morphology quality of the printed part.

(2). Through Taguchi experiments and SNR analysis, the impact of process parameters on the individual response of  $\Delta H$  is  $SS > PR > LP > SD$ . The effect on the individual response of  $Ra$  is  $SD > PR > SS > LP$ . The influence of process parameters on the multi-objective response obtained using the grey relational analysis method is  $SD > PR > SS > LP$ . The optimal parameter combination was determined to be LP1PR1SD3SS3. That is to say, the laser power is 800 W, the

powder feeding rate is 0.3 r/min, the step distance is 1.6 mm, and the scanning speed is 20 mm/s.

(3). Considering the multifactorial characteristics of the metal powder LDED process, the GB-BP network was designed to predict the  $\Delta H$  and  $Ra$  of printed parts to improve manufacturing efficiency. The BO algorithm determines the ideal number of hidden layers and nodes for the BP network, while GA replaces the backpropagation process to improve its performance. Through experimental verification, the GB-BP network significantly improves prediction accuracy compared to the traditional BP network, with  $\Delta H$  and  $Ra$  prediction accuracy increasing by 43.14% and 71.43%, respectively.

The following research will focus on expanding the dataset and refining the network, aiming to improve the accuracy of multi-target response in multi-layer and multi-pass metal printed parts.

### References

- Guo N, Leu M C. *Frontiers of mechanical engineering*[J], 2013, 8: 215-243.
- Dawood A, Marti B M, Sauret-Jackson V, et al. *British dental journal* [J], 2015, 219(11): 521-529.

- 3 Gradl P R, Protz C S, Wammen T. *AIAA Propulsion and Energy 2019 Forum*[C], 2019: 4362.
- 4 Fan Y, Lin Y, Ao Q, et al. *Rare Metal Materials and Engineering*[J], 2023, 52(10): 3630-3639.
- 5 Zhang J, Zhang Q, Chen Z, et al. *Journal of Laser Applications*[J], 2019, 31(3).
- 6 Kistler N A, Nassar A R, Reutzel E W, et al. *Journal of Laser Applications*[J], 2017, 29(2).
- 7 Hussain M, Kumar V, Mandal V, et al. *Materials and Manufacturing Processes*[J], 2017, 32(14): 1667-1677.
- 8 Mondal S, Bandyopadhyay A, Pal P K. *The International Journal of Advanced Manufacturing Technology*[J], 2014, 70: 2151-2158.
- 9 Lin J L, Lin C L. *International Journal of machine Tools and manufacture*[J], 2002, 42(2): 237-244.
- 10 Tsai M J, Li C H. *Optics & Laser Technology*[J], 2009, 41(8): 914-921.
- 11 Fu C, Zheng J, Zhao J, et al. *Corrosion Science*[J], 2001, 43(5): 881-889.
- 12 Ge W, Guo C, Lin F, et al. *Rare Metal Materials and Engineering*[J], 2015, 44(11): 2623-2627.
- 13 Javid Y. *CIRP Journal of Manufacturing Science and Technology*[J], 2020, 31: 406-417.
- 14 Fatoba O S, Akinlabi E T, Akinlabi S A, et al. *Materials Today: Proceedings*[J], 2018, 5(9): 19181-19190.
- 15 Marzban J, Ghaseminejad P, Ahmadzadeh M H, et al. *The International Journal of Advanced Manufacturing Technology*[J], 2015, 76: 1163-1172.
- 16 Deng D, Li T, Huang Z, et al. *Optics & Laser Technology*[J], 2022, 153: 108259.
- 17 Mondal S, Paul C P, Kukreja L M, et al. *The International Journal of Advanced Manufacturing Technology*[J], 2013, 66: 91-96.
- 18 Quazi M M, Fazal M A, Haseeb A, et al. *Tribology Transactions*[J], 2017, 60(2): 249-259.
- 19 Yu T, Yang L, Zhao Y, et al. *Optics & Laser Technology*[J], 2018, 108: 321-332.
- 20 Lian G, Zhao C, Zhang Y, et al. *Applied Sciences*[J], 2020, 10(9): 3167.
- 21 Lee E M, Shin G Y, Yoon H S, et al. *Journal of Mechanical Science and Technology*[J], 2017, 31: 3411-3418.
- 22 Alam M K, Urbanic R J, Nazemi N, et al. *The International Journal of Advanced Manufacturing Technology*[J], 2018, 94: 397-413.
- 23 Bhardwaj T, Shukla M, Paul C P, et al. *Journal of Alloys and Compounds*[J], 2019, 787: 1238-1248.
- 24 Yin F, Mao H, Hua L. *Materials & Design*[J], 2011, 32(6): 3457-3464.
- 25 Mohajernia B, Mirazimzadeh S E, Pasha A, et al. *The International Journal of Advanced Manufacturing Technology* [J], 2022: 1-20.
- 26 Li Y, Wang K, Fu H, et al. *Coatings*[J], 2021, 11(11): 1402.
- 27 Lestan Z, Klancnik S, Balic J, et al. *Materials and Manufacturing Processes*[J], 2015, 30(4): 458-463.
- 28 Ilanlou M, Razavi R S, Nourollahi A, et al. *Optics & Laser Technology*[J], 2022, 156: 108507.
- 29 YANG Y, TIAN Z, PAN H, et al. *TRANSACTIONS OF THE CHINA WELDING INSTITUTION*[J], 2013 (11): 78-82.
- 30 Liu H, Qin X, Huang S, et al. *International Journal of Precision Engineering and Manufacturing*[J], 2018, 19: 1061-1070.
- 31 Yu J, Sun W, Huang H, et al. *Coatings*[J], 2019, 9(11): 728.
- 32 Deng Z, Chen T, Wang H, et al. *Applied Sciences*[J], 2020, 10(18): 6331.
- 33 Wang S, Zhu L, Fuh J Y H, et al. *Optics and Lasers in Engineering*[J], 2020, 127: 105950.
- 34 Kumar P, Jain N K, Sawant M S. *Journal of Materials Research and Technology*[J], 2022, 17: 95-110.
- 35 Ahmed N, Barsoum I, Haidemenopoulos G, et al. *Journal of Manufacturing Processes*[J], 2022, 75: 415-434.
- 36 Zhang Y, Xu Y, Sun Y, et al. *Surface Topography: Metrology and Properties*[J], 2022, 10(4): 044007.
- 37 Lian G, Zhang H, Zhang Y, et al. *Coatings*[J], 2019, 9(6): 356.
- 38 Lian G, Xiao S, Zhang Y, et al. *The International Journal of Advanced Manufacturing Technology*[J], 2021, 112: 1449-1459.
- 39 Okuyucu H, Kurt A, Arcaklioglu E. *Materials & design*[J], 2007, 28(1): 78-84.
- 40 Li Y, Liu Y, Luo S, et al. *Journal of Materials Research and Technology*[J], 2020, 9(6): 14467-14477.
- 41 Snoek J, Larochelle H, Adams R P. *Advances in neural information processing systems*[J], 2012, 25.
- 42 Ding S, Su C, Yu J. *Artificial intelligence review*[J], 2011, 36: 153-162.
- 43 Wong T T. *Pattern recognition*[J], 2015, 48(9): 2839-2846.
- 44 Li H, Wu D, Wang H. *Measurement*[J], 2025, 242: 115732.

## 多层多道次 LDED 工艺参数智能决策与多目标预测

李亚冠<sup>1,2</sup>, 聂振国<sup>2,3,4</sup>, 李荟林<sup>2</sup>, 王涛<sup>1</sup>, 黄庆学<sup>1</sup>

(1. 太原理工大学 机械工程学院, 山西 太原 030024)

(2. 清华大学 机械工程系, 北京 100084)

(3. 清华大学 先进装备摩擦学国家重点实验室, 北京 100084)

(4. 清华大学 精密超精密制造装备与控制北京市重点实验室, 北京 100084)

**摘要:** 表征多层多道次激光金属打印件形貌质量的主要参数是表面粗糙度和实际打印高度与理论模型高度之间的误差。本研究采用田口法建立工艺参数组合与金属打印形貌质量(高度误差和粗糙度)多目标表征之间的关联性。采用信噪比和灰色关联分析法预测多层多道次打印的最优参数组合:激光功率 800 W、送粉速率 0.3 r/min、步距 1.6 mm、扫描速度 20 mm/s。随后,构建遗传贝叶斯-反向传播网络(GB-BP)对多目标响应进行预测。与传统 BP 网络相比,GB-BP 网络对高度误差和表面粗糙度的预测精度分别提高了 43.14%和 71.43%,该网络可以准确预测多层多道次 LDED 金属打印部件的形貌和质量的多目标表征。

**关键词:** 多层多道次激光熔覆;田口法;灰色关联分析;GB-BP网络

作者简介:李亚冠,男,1995年生,博士研究生,太原理工大学机械工程学院,山西太原 030024, E-mail: liyaguan0014@link.tyut.edu.cn